aerospace

MDPI

Article

Tailoring 3D Star-Shaped Auxetic Structures for Enhanced Mechanical Performance

Yulong Wang [1], Naser A. Alsaleh [2], Joy Djuansjah [2], Hany Hassanin [3,*], Mahmoud Ahmed El-Sayed [4] and Khamis Essa [1,*]

[1] Department of Mechanical Engineering, University of Birmingham, Birmingham B15 2TT, UK
[2] Department of Mechanical Engineering, Imam Mohammad Ibn Saud Islamic University (IMSIU), Riyadh 11432, Saudi Arabia
[3] School of Engineering, Technology, and Design, Canterbury Christ Church University, Canterbury B15 2TT, UK
[4] Department of Industrial and Management Engineering, Arab Academy for Science Technology and Maritime Transport, Alexandria 21599, Egypt; dr.mahmoudelsayed12@gmail.com
* Correspondence: hany.hassanin@canterbury.ac.uk (H.H.); k.e.a.essa@bham.ac.uk (K.E.)

Abstract: Auxetic lattice structures are three-dimensionally designed intricately repeating units with multifunctionality in three-dimensional space, especially with the emergence of additive manufacturing (AM) technologies. In aerospace applications, these structures have potential for use in high-performance lightweight components, contributing to enhanced efficiency. This paper investigates the design, numerical simulation, manufacturing, and testing of three-dimensional (3D) star-shaped lattice structures with tailored mechanical properties. Finite element analysis (FEA) was employed to examine the effect of a lattice unit's vertex angle and strut diameter on the lattice structure's Poisson's ratio and effective elastic modulus. The strut diameter was altered from 0.2 to 1 mm, while the star-shaped vertex angle was adjusted from 15 to 90 degrees. Laser powder bed fusion (LPBF), an AM technique, was employed to experimentally fabricate 3D star-shaped honeycomb structures made of Ti_6Al_4V alloy, which were then subjected to compression testing to verify the modelling results. The effective elastic modulus was shown to decrease when increasing the vertex angle or decreasing the strut diameter, while the Poisson's ratio had a complex behaviour depending on the geometrical characteristics of the structure. By tailoring the unit vertex angle and strut diameter, the printed structures exhibited negative, zero, and positive Poisson's ratios, making them applicable across a wide range of aerospace components such as impact absorption systems, aircraft wings, fuselage sections, landing gear, and engine mounts. This optimization will support the growing demand for lightweight structures across the aerospace sector.

Keywords: star-shaped lattice structure; auxetic structures; laser powder bed fusion; Poisson's ratio

Citation: Wang, Y.; Alsaleh, N.A.; Djuansjah, J.; Hassanin, H.; El-Sayed, M.A.; Essa, K. Tailoring 3D Star-Shaped Auxetic Structures for Enhanced Mechanical Performance. *Aerospace* **2024**, *11*, 428. https://doi.org/10.3390/aerospace11060428

Received: 30 April 2024
Revised: 18 May 2024
Accepted: 22 May 2024
Published: 24 May 2024

1. Introduction

Materials with zero or negative properties represent a paradigm shift by challenging conventions of traditional materials and introducing novel characteristics. Historically, properties such as thermal expansion, refractive indices, Poisson's ratio, permittivity, permeability, compressibility, and stiffness have all shown positive values. For an airplane subjected to significant temperature variations, materials with negative thermal expansion coefficients present prospects for the development of lightweight components with increased thermal stability. Additionally, materials with negative refractive indices may have potential for used in designing small, effective antennas that reduce overall weight and size while improving radar and communication capabilities. This potential makes them suitable for aerospace applications where efficiency, performance, and weight are essential considerations [1]. Metamaterials have attracted substantial research attention during the past few years as an emerging concept for developing materials with novel properties different from those of conventional materials [2]. Metamaterials, or

engineered materials, have designed properties that can be tailored to control the values of Poisson's ratio and permeability, permittivity, and refractive index properties, allowing achieving negative values through creating designed pores. Auxetic materials, one type of metamaterial, were shown to exhibit the very unusual property of becoming wider when stretched and narrower when compressed. This property gives a material several beneficial properties, such as increased shear stiffness, increased plane strain fracture toughness, increased indentation resistance, and improved acoustic damping properties [3]. Open-celled porous structure metamaterials called lattice structures provide a special combination of high functionality and low weight. They facilitate the production of engineered components with tailored properties such as high specific strength and high toughness [4,5]. The low relative density as well as high surface area of such structures allow their use in filters, catalytic convertors, armour, heat exchangers, load-bearing components, biomedical implants, and so on.

Poisson's ratio is a fundamental mechanical property that reflects the structural deformation being applied perpendicular to the applied force. Typically, most conventional materials have positive Poisson's ratios, which means these materials expand (or contract) laterally when subjected to axial compressive (or tensile) stresses. One of the unique properties of lattice structures is that it allows the control of a material's Poisson's ratio to facilitate the acquisition of negative values, as in auxetic structures [6]. Materials with a negative Poisson's ratio, known as "auxetic", can contract (or expand) laterally when compressed (or stretched) axially [7]. Human tissues such as trabecular bones and specific ligaments; liquid crystalline polymers; and egg rack structures are examples of this type of structure [8–10]. Auxetic structures were classified into three categories by Kim et al. [11] according to the characteristics that produce the auxetic effect: re-entrant, chiral, and spinning.

Additive manufacturing technologies have emerged as an innovative industrial solution in recent decades, expanding to a wide range of applications. This is because of their ability to be used in manufacturing complex shapes and customised designs that are challenging to achieve using traditional technologies [12,13]. For all AM techniques, creating three-dimensional structures from a digitally created CAD model is achieved through the layer-by-layer printing of materials. One of the most advanced AM processes, laser powder bed fusion (LPBF), was developed in the latter half of the 1980s, adhering to ASTM F2792 [14]. It is a solid freeform manufacturing process used to create three-dimensional objects via laser scanning a powder bed layer in an inert environment. Using a recoater blade, LPBF is used to apply a thin layer of metal powder to a building substrate. The powder is then melted, and a liquid melt pool is created by the laser beam scanning the predetermined path of the CAD model. After cooling, the molten pool turns into a layer of the component. Once the substrate's height is reduced by one layer, the procedure is restarted and carried out again until the component is fully printed [15,16]. The development of lattice structures with intricate internal porosity and voids intended to exhibit certain mechanical and physical characteristics has been made possible by the advent of LPBF, which is widely used in the manufacturing of 2D, 2.5D, and 3D lattice structures, including zero-Poisson's ratio (ZPR) and auxetic materials, due to their special deformation properties [17,18].

Zadeh et al. [19] developed a 2D lattice structure dubbed Fish Cells, which was shown to have a Poisson's ratio of zero, and suggested that it can be efficiently employed for skin morphing. In another study, Gong et al. proposed a 3D zero-Poisson's ratio lattice structures that showed lightweight and out-of-plane rigidity [20]. Negative-Poisson's ratio or auxetic structures have also been studied since they are designed to have superior energy absorption capabilities, making them useful for impact protection and vibration dampening. Recent research has also found that various human body sections, including muscle, ligament, vascular, and skin tissues, exhibit negative Poisson's ratios [11]. The re-entrant structure, in both 2D and 3D configurations, is one of the most well-established auxetic structure types. This structure has been shown to have important characteristics for

several applications, including impact-resistant materials, flexible electronics, and biomedical implants [21,22].

Yang et al. [22] created 3D re-entrant auxetic structures based on their original 2D geometries and investigated their compressive properties and Poisson' ratios as the geometry of the unit cell changed. The authors found that considerable variations in effective modulus and compressive strength were exhibited when the structures were compressed in different directions. In another study, Rad et al. [23] created 3D star structures that can have a negative Poisson's ratio in all directions if the unit cell design parameters are kept within a certain range. They found that the Poisson's ratio and elastic modulus were correlated with the design parameters but limited in range variabilities since they only included one type of unit cell. By combining various unit cell types, structures with a wide variety of Poisson's ratios and compressive characteristics ranges might be achieved.

Several other research works have also been presented. Strek et al. [24] reported that there was a significant influence of Poisson's ratio on contact pressure between a half-cylinder elastic body and a clamped plate. Mrozek et al. [25] showed that the dynamic behaviour of an auxetic material could also be enhanced by adjusting the geometric parameter of its structure. In addition, the results obtained by Bilski et al. [26] demonstrated a strong correlation between the geometry of 2D lattice structures and the resulting Poisson's ratio.

The reviewed research has shown that 3D auxetic materials exhibit promising capabilities. However, there is a gap in research regarding structural designs capable of maintaining their negative Poisson's properties under varying loading directions. There is a need to find a structure that exhibits true auxetic behaviour in all three orthogonal axes. Therefore, the goal of this study is to introduce a 3D star-shaped lattice structure with isotropic mechanical properties. The developed star-shaped lattice structure was characterised using finite element analysis, as well as mechanical testing, to explore the effect of vertex angle (θ) and strut diameter (D) on the Poisson's ratio (ν) and the effective elastic modulus (E/E^*) of the structure, where E and E^* are the elastic moduli of a structure and its building material, respectively. The effective elastic modulus ratio represents the relative stiffness of the star-shaped lattice structure relative to the solid material when it has full density.

2. Methodology

Figure 1 depicts the flow chart used to evaluate the mechanical characteristics of the star-shaped lattice structure. Initially, the geometrical parameters, specifically the vertex angle and strut diameter, were specified. CAD drawings were then created using these parameters. Next, geometric models of the samples were generated, and their mechanical characteristics were evaluated using finite element analysis (FEA). Finally, the FEA findings were evaluated against experimental data. In addition, this process included two feedback loops: one to evaluate the minimum representative volume element (RVE) and another to perform mesh sensitivity analysis.

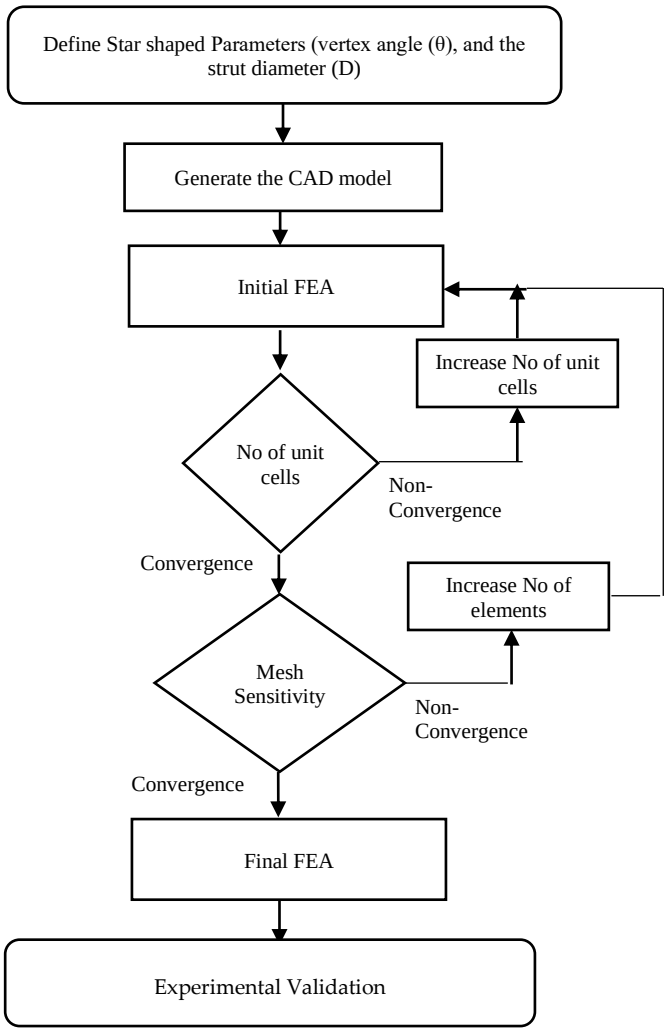

Figure 1. Flow chart of the methodology applied for the assessment of the mechanical properties of star-shaped structures.

2.1. Star-Shaped Design

The methods used to evaluate the mechanical properties of the star-shaped lattice structure are described below, beginning with the design of the structure. Lattice structures are designed with repeated and joined unit cells with a specific geometric arrangement. For a 3D star-shaped lattice structure, the unit cell is made up of struts or beams arranged in a star-like shape. Each strut extends outward from a centre point, like a star or an asterisk. The repeated struts meet at various locations, resulting in a network of linked units that create the lattice structure, as shown in Figure 2a.

As indicated above, this design focused on varying two essential geometrical parameters, namely, the vertex angle (θ) and the strut diameter (D), as shown in Figure 2b. Each unit cell is 14 × 14 × 14 mm^3. The two parameters were investigated in the ranges of 15 to 90° for the vertex angle (six identical levels) and 0.2 to 1.0 mm for the strut diameter (nine equal levels). Ti_6Al_4V alloy was chosen for use in the star-shaped lattice structure due to its outstanding mechanical strength, lightweight nature, and excellent corrosion resistance. This alloy is commonly utilised in aerospace, automotive, and biomedical applications, making it a dependable material for engineering constructions that require high performance and endurance.

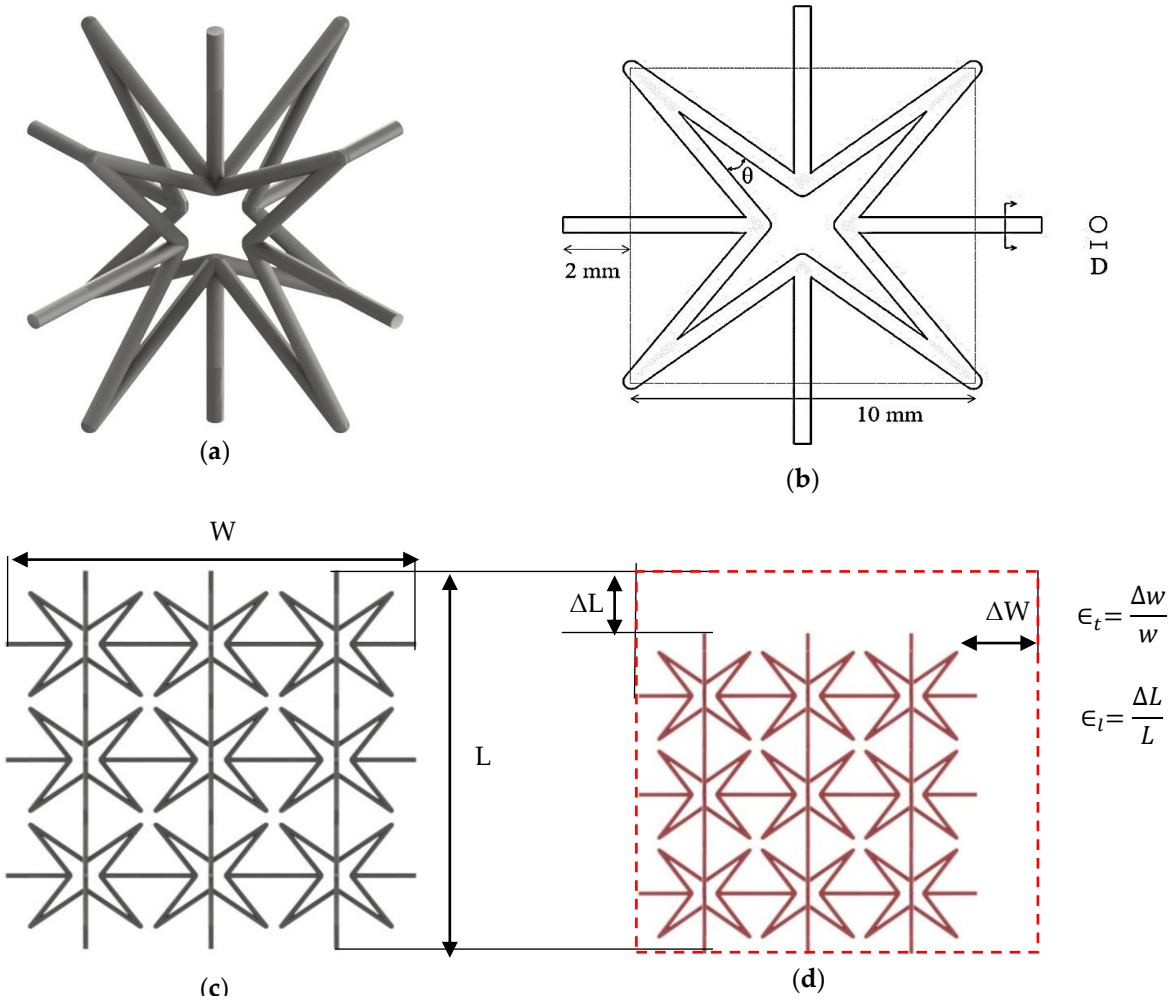

Figure 2. (**a**) lattice structure; (**b**) design parameters; (**c**) before compression; (**d**) after compression.

2.2. Calculation of Elastic Modulus and Poisson's Ratio

The stress–strain data obtained from the FEA simulations were used to compute the elastic modulus (E) of the star-shaped lattice structures. The slope of the stress–strain curve within the linear elastic zone was used to compute the elastic modulus by dividing the change in stress (Δσ) by the change in strain (Δε), as shown in Equation (1):

$$E = \frac{\Delta\sigma}{\Delta\epsilon} \quad (1)$$

The elastic modulus, Poisson's ratio, and yield strength of the Ti_6Al_4V alloy are 113.8 GPa, 0.342, and 1000 MPa, respectively *[27–29]*. In this study, the effective elastic modulus of the structure was calculated by dividing its elastic modulus by that of the solid Ti_6Al_4V alloy. The Poisson's ratio (v) was determined by first computing the average displacement of the ends of the laterally projecting struts. Then, the transverse strain ϵ_t corresponding to this displacement was divided by the longitudinal contraction strain ϵ_l in the direction of the stretching force to obtain the Poisson's ratio (see Equation (2)). Figure 2c,d show graphical representations of the determination of the elastic modulus and Poisson's ratio, respectively.

$$\nu = \frac{-\epsilon_t}{\epsilon_l} \quad (2)$$

2.3. Numerical Modelling

The geometry of the star-shaped lattice structure was created in Solidworks 2018 (Dassault Systems, Velizy-Vilacoublau, France), as shown in Figure 2. A total of 54 samples with different strut diameters and vertex angles were designed to investigate the effects of the geometrical parameters of the star-shaped lattice structures under investigation on their mechanical properties. Next, the samples were imported into Abaqus 2017 (Dassault Systemes, Velizy-Vilacoublau, France) for finite element analysis. The minimal representative volume element (RVE) of the star-shaped lattice structure was determined through an initial investigation in order to save the computation time of the FEA [30]. The FEA was performed with models that ranged in unit cell count from 1 × 1 × 1 (one single unit cell) to a maximum of 5 × 5 × 5 (125 unit cells). After assessing the convergence of the FEA results, the lowest number of unit cells that adequately represent the model was identified.

Because of the symmetry of the model, the top and bottom faces of the model were constrained by reference points in the loading direction (z-axis). Applying a 2.1 mm displacement, or 5% strain, to the top reference point allowed the creation of a star-shaped lattice structure. Here, 5% strain was chosen to allow us to apply significant deformation to enable an assessment of how the structure responds while avoiding excessive deformation that might compromise its integrity. An extra point was selected and constrained in the x direction to ensure sufficient restriction of the deformation of the model (see Figure 3a). It is worth noting that the above boundary conditions are appropriate for the current small and finite number of unit cells. For a large or infinite number of unit cells, it is appropriate to apply periodic boundary conditions. Periodic boundary conditions offer several advantages as they allow for the modelling of infinite periodic lattice structures; this makes it easier to comprehend the mechanical properties and scaling behaviour of lattice structures in large dimensions. Periodic boundary conditions eliminate border interactions and edge effects that may arise in small samples, making the lattice structure's behaviour uniform.

Finally, a mesh sensitivity analysis was performed to ensure that the results converged with the allocated number of elements, aiming to achieve a result variation lower than 0.1%. To compare and assess the simulation results with various mesh sizes, the element size range was set to 0.33d to 0.5d of the strut diameters. An optimal element size was identified by investigating the convergence of the results and the computing time (see Figure 3b).

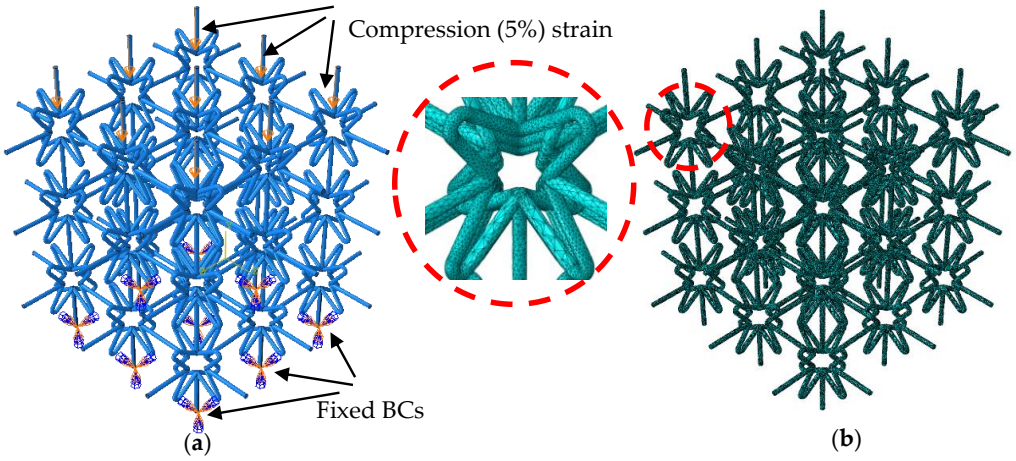

Figure 3. (**a**) Boundary conditions; (**b**) an example of the meshing.

2.4. Experimental

Three star-shaped lattice structures with various strut diameters and vertex angles were printed in order to verify the computational model results. The chosen designs had the following geometrical parameters: θ = 75 and D = 0.5 mm, θ = 50° and D = 0.5 mm, and θ = 40° and D = 0.5 mm. Ti_6Al_4V gas-atomized titanium alloy powder with a particle size of d_{50} = 40 μm was provided by TLS Technik GmbH (Bitterfeld-Wolfen, Germany). Characterization of the particle size distribution of the Ti_6Al_4V powder was carried out according to the ASTM B822 standard [31] using a laser diffraction analyser (Microtrac, Microtrac Retsch GmbH, Haan, Germany). The powder was found to have good flowability, as shown by its Hausner ratio of 1.16. The 3D star-shaped lattice structures were then fabricated using the Renishaw RenAM 500 M LPBF system (Renishaw plc, Wot ton-under-Edge, UK). The LPBF process was carried out within an argon environment in the building unit using a Renishaw machine with an oxygen concentration less than 0.1% and standard process parameters for Ti_6Al_4V consisting of 200 W of laser power, a 1200 mm/s scanning speed, and a layer thickness 0.02 mm for.

The building direction of the 3D star-shaped lattice structures had to be optimally oriented at ideal angles to avoid producing horizontal and shallow-angle printed struts, which could lead to overhanging problems and weak adhesion with the substrate during printing [32]. The designs were rotated 45° about the y-axis and then 45° about the x-axis in order to achieve the best building orientation (Figure 4a). To further support the overhung struts, internal supports needed to be placed (Figure 4b). Nevertheless, because the locations of these supports were difficult to access, their removal was found difficult. As a result, the supports were made much thinner than the original struts in order to address this issue and facilitate the removal process. Zwick/Roell (Zwick Roell Group, Zwick GmbH, Ulm, Germany) universal testing equipment was utilised to assess the compression properties of the fabricated samples, using a compression rate of 1 mm/min, and the results were used to calculate the Poisson's ratios and effective elastic moduli of the as-fabricated samples. To guarantee a uniform distribution of the compressive force throughout the test, the structures were positioned at the middle of the loading plate.

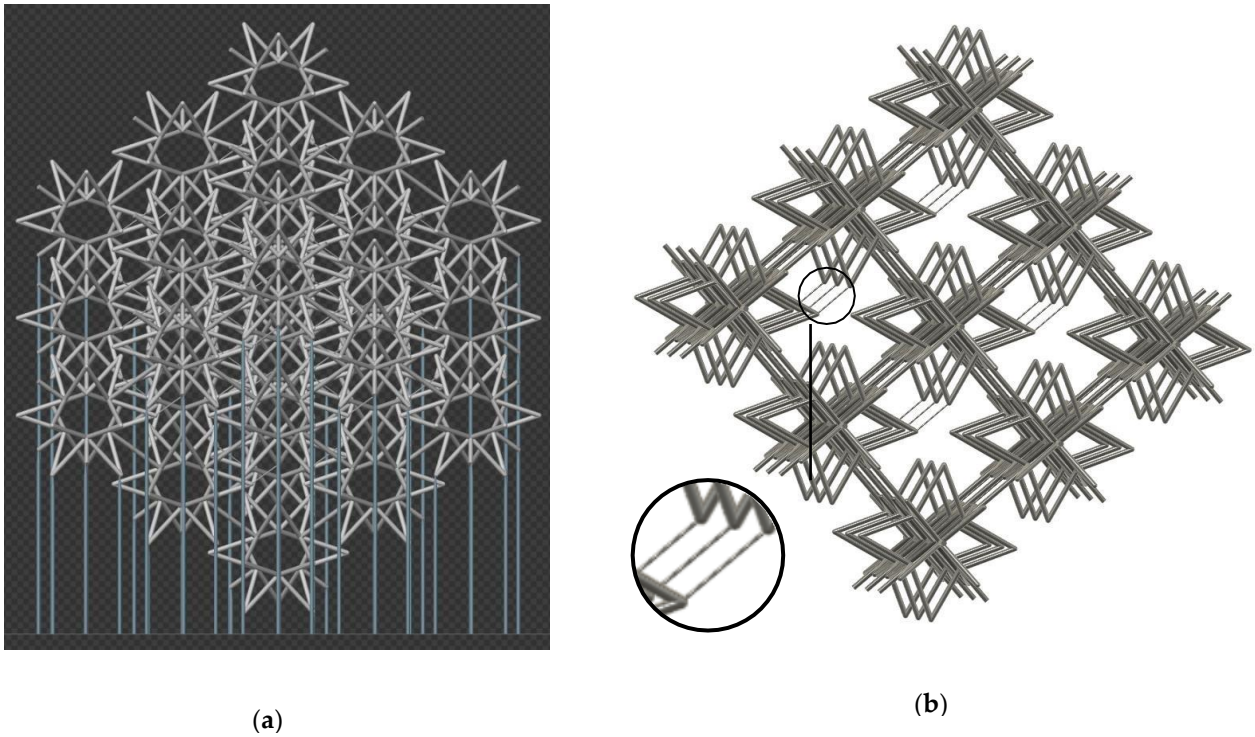

(**a**) (**b**)

Figure 4. (**a**) Printing position of the structure; (**b**) structure with internal support added.

3. Results and Discussion

3.1. Modelling

The results of the preliminary simulations used to calculate the lowest representative volume element are shown in Figure 5. This figure shows the effect of the star-shaped lattice structure unit cells on both the Poisson's ratio and effective elastic modulus. For both properties, it was observed that convergence started when the design of the lattice structure had at least 8 unit cells (2 × 2 × 2). Based on these results, it was decided that the design of the star-shaped lattice structures considered in this study, both computationally and experimentally, should have 27 unit cells 3 × 3 × 3. Figure 6 shows an FEA example of this setup before and after compression, demonstrating typical negative-Poisson's ratio behaviour. In this figure, u represents deformation under compression, while u1 indicates deformation in the x-direction.

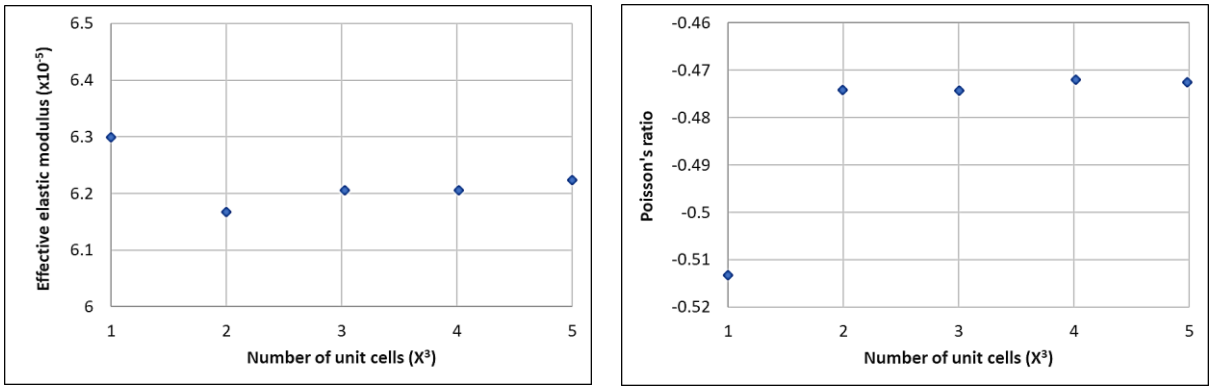

(**a**) (**b**)

Figure 5. Convergence of simulation results against the number of unit cells for (**a**) effective elastic modulus and (**b**) Poisson's ratio.

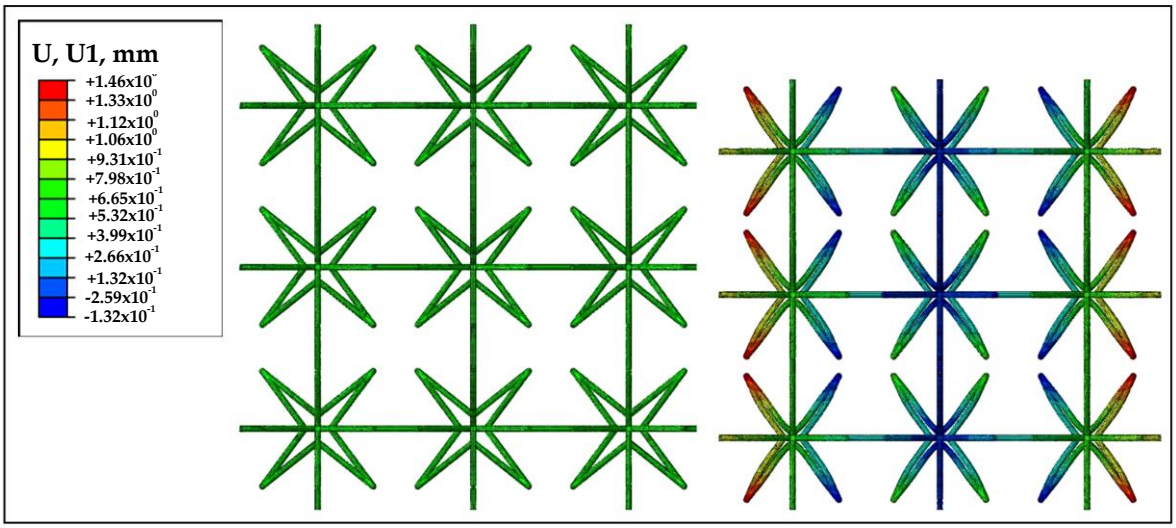

(**a**) (**b**)

Figure 6. Compression of the 3 × 3 × 3 model in FEA (**a**) before compression and (**b**) after compression.

Table 1 and Figure 7 show the mesh sensitivity analysis findings for the 3D star-shaped lattice model with a vertex angle of 75° and a strut diameter of 0.5 mm. The FEA simulation results for both the Poisson's ratio and the effective elastic modulus began to converge when the element size was about 0.17 mm (which is about one-third of the strut

diameter). This indicates that more mesh refinement beyond this stage would not have any meaningful effects on the accuracy or precision of the simulation results while simultaneously consuming more computing processing time. As a result, the element size of the FEA models was determined to be one-third of the strut diameter.

Table 1. Mesh sensitivity analysis on a model with (θ = 75°, D = 0.5 mm).

Element Size (mm)	Number of Elements	Poisson's Ratio	Effective Elastic Modulus (×10⁻⁵)
0.25	130,984	0.1623	2.432
0.23	137,271	0.1622	2.432
0.21	198,777	0.1617	2.426
0.19	230,337	0.1614	2.422
0.167	295,819	0.1606	2.412
0.15	362,941	0.1606	2.411

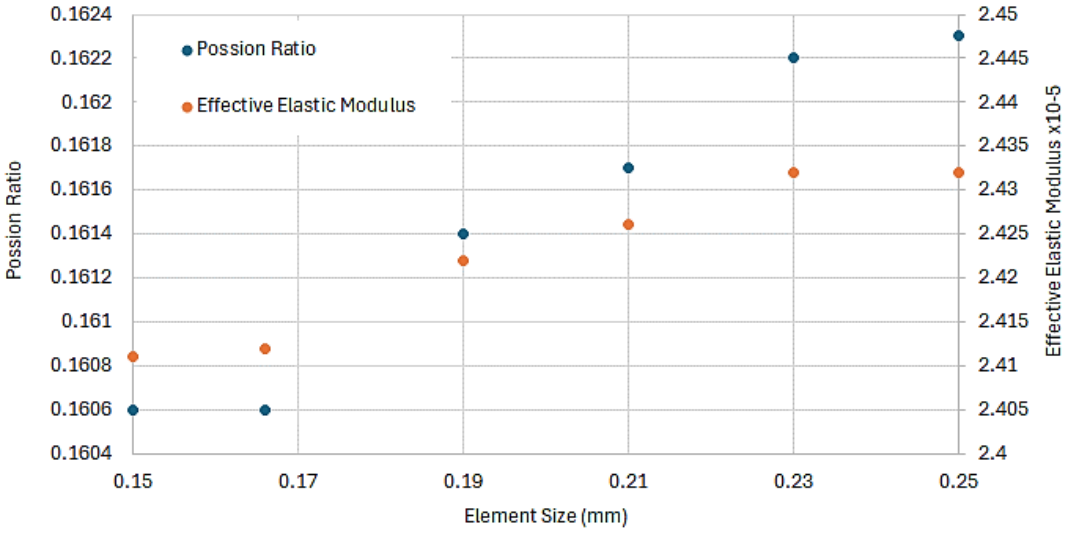

Figure 7. The mesh convergence behaviour results for a model with (θ = 75°, D = 0.5mm).

The FEA results, listed in Table 2 and shown graphically in Figure 8, show a clear trend in which the effective elastic moduli drop as the vertex angle increases or strut diameter decreases. This shows that if the vertex angle increases or the strut diameter decreases, the lattice structure's stiffness decreases. Furthermore, the relationship between Poisson's ratio and strut diameter varies depending on the vertex angle. For star-shaped lattice structures with vertex angles greater than 60°, there is an inverse relationship between the Poisson's ratio and the strut diameter. In contrast, lattice structures with vertex angles less than 60° exhibit a direct relationship. In general, star-shaped lattice structures with smaller angles have lower Poisson's ratios, except for those for which D = 1 mm, which showed a minor reduction in Poisson's ratio as the vertex angle increased. This is because in designs with large strut diameters but small vertex angles, the centre hollow area becomes too constrained to allow the horizontal struts to contract until 5% strain is reached. As a result, the struts attached to the same vertex come into complete contact with one another, leading to a material's yielding.

Table 2. Simulation results regarding the star-shaped lattice structure.

Θ (°)	D (CAD) (mm)	ν	E/E^*	Θ (°)	D (CAD) (mm)	ν	E/E^*
15	0.2	−0.798	1.06×10^{-6}	60	0.6	0.086	5.49×10^{-5}
30	0.2	−0.379	8.01×10^{-7}	75	0.6	0.157	5.22×10^{-5}

45	0.2	−0.09	6.71×10^{-7}	90	0.6	0.198	5.23×10^{-5}
60	0.2	0.069	6.08×10^{-7}	15	0.7	−0.329	3.26×10^{-4}
75	0.2	0.16	5.98×10^{-7}	30	0.7	−0.169	1.57×10^{-4}
90	0.2	0.212	6.06×10^{-7}	45	0.7	−0.028	1.19×10^{-4}
15	0.3	−0.713	6.17×10^{-6}	60	0.7	0.089	1.04×10^{-4}
30	0.3	−0.341	4.23×10^{-6}	75	0.7	0.153	9.82×10^{-5}
45	0.3	−0.077	3.51×10^{-6}	90	0.7	0.192	9.82×10^{-5}
60	0.3	0.075	3.20×10^{-6}	15	0.8	−0.22	6.30×10^{-4}
75	0.3	0.166	3.09×10^{-6}	30	0.8	−0.136	2.81×10^{-4}
90	0.3	0.21	3.12×10^{-6}	45	0.8	−0.02	2.09×10^{-4}
15	0.4	−0.637	2.27×10^{-5}	60	0.8	0.091	1.81×10^{-4}
30	0.4	−0.295	1.43×10^{-5}	75	0.8	0.148	1.70×10^{-4}
45	0.4	−0.063	1.14×10^{-5}	90	0.8	0.186	1.70×10^{-4}
60	0.4	0.079	1.03×10^{-5}	15	0.9	−0.126	1.13×10^{-3}
75	0.4	0.164	9.91×10^{-6}	30	0.9	−0.108	4.70×10^{-4}
90	0.4	0.208	1.00×10^{-5}	45	0.9	−0.014	3.43×10^{-4}
15	0.5	−0.551	6.45×10^{-5}	60	0.9	0.089	2.95×10^{-4}
30	0.5	−0.246	3.70×10^{-5}	75	0.9	0.144	2.76×10^{-4}
45	0.5	−0.049	2.91×10^{-5}	90	0.9	0.181	2.75×10^{-4}
60	0.5	0.083	2.58×10^{-5}	15	1	−0.067	1.89×10^{-3}
75	0.5	0.161	2.47×10^{-5}	30	1	−0.081	7.46×10^{-4}
90	0.5	0.204	2.49×10^{-5}	45	1	−0.007	5.37×10^{-4}
15	0.6	−0.399	1.55×10^{-4}	60	1	0.086	4.58×10^{-4}
30	0.6	−0.203	8.10×10^{-5}	75	1	0.141	4.27×10^{-4}
45	0.6	−0.039	6.24×10^{-5}	90	1	0.176	4.23×10^{-4}

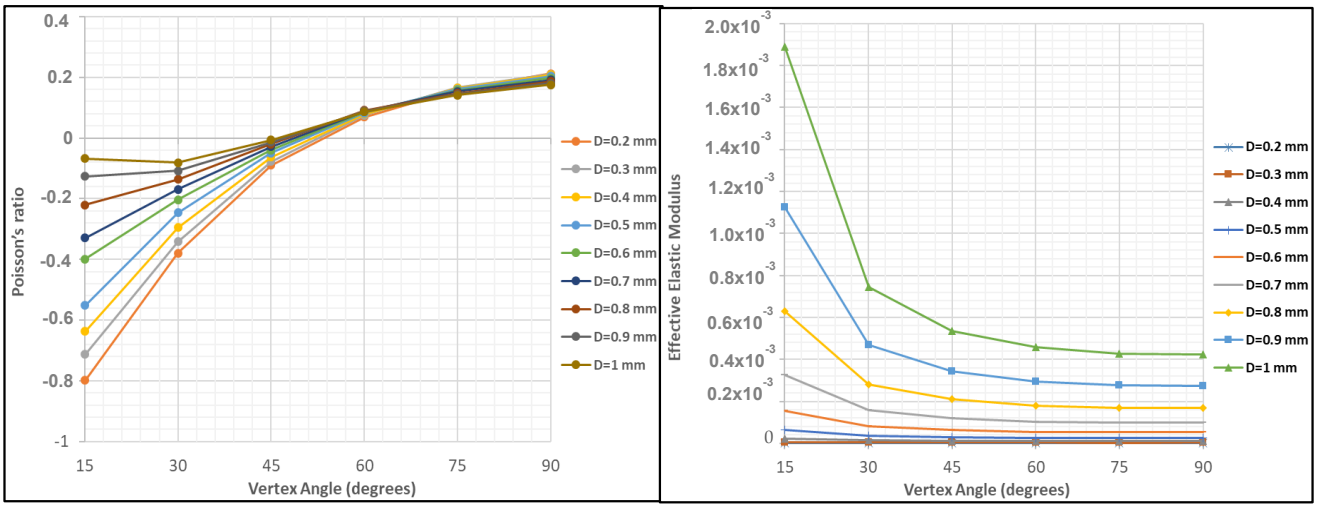

(a) (b)

Figure 8. Plots of (**a**) Poisson's ratio and (**b**) effective elastic modulus against vertex angle for different strut diameters.

Least squares fitting, which is a mathematical procedure used for finding the best-fitting curve to a given set of points by minimizing the sum of the squares of the offsets of the points from the curve, was applied to analyse the data presented in Table 2. In this way, the relationship between the design parameters (strut diameter and vertex angle) and the Poisson's ratio and effective elastic modulus of the star-shaped lattice structure were determined. The coefficient of correlation (R^2) is used to describe model fit in regression analysis. Based on the model fitting, the fourth-degree polynomial function was found to be the most suitable model for both properties. Equations (3) and (4) provide the general empirical formulae that express the Poisson's ratio as well as the effective elastic modulus, respectively, in terms of the strut diameter and vertex angle:

$$\nu = f(\theta, D) = a_{00} + a_{10}\theta + a_{01}D + a_{20}\theta^2 + a_{11}\theta D + a_{02}D^2 + a_{30}\theta^3 + a_{21}\theta^2 D + a_{12}\theta D^2 + a_{03}D^3 + a_{40}\theta^4 + a_{31}\theta^3 D + a_{22}\theta^2 D^2 + a_{13}\theta D^3 + a_{04}D^4 \quad (3)$$

$$E/E^* = g(\theta, D) = b_{00} + b_{10}\theta + b_{01}D + b_{20}\theta^2 + b_{11}\theta D + b_{02}D^2 + b_{30}\theta^3 + b_{21}\theta^2 D + b_{12}\theta D^2 + b_{03}D^3 + b_{40}\theta^4 + b_{31}\theta^3 D + b_{22}\theta^2 D^2 + b_{13}\theta D^3 + b_{04}D^4 \quad (4)$$

where the model coefficients, a_{ij} and b_{ij}, are provided in Table 3 and were determined by an examination of the data using the least-squares fitting method. The coefficient of determination (R^2) values for various polynomial orders were examined, and we ultimately chose a fourth-order polynomial model as it was more accurate compared to those of lower orders. The fits in the current investigation showed strong R^2 values for the effective elastic modulus and Poisson's ratio, amounting to 0.9875 and 0.9992, respectively. These values show a very high goodness of fit. Figures 8 and 9 show charts displaying these fitted functions for the Poisson's ratio and effective elastic modulus as a function of the strut diameter and vertex angle.

Table 3. Values of the coefficients a_{ij} and b_{ij} in Equations (3) and (4).

i	j	a_{ij}	b_{ij}	i	j	a_{ij}	b_{ij}
0	0	3.27×10^{-2}	7.6×10^{-5}	1	2	1.298×10^{-3} (m^{-2} rad^{-1})	-7.533×10^{-5} (m^{-2} rad^{-1})
1	0	2.13×10^{-1} (rad^{-1})	6.38×10^{-5} (rad^{-1})	0	3	-3.355×10^{-3} (m^{-3})	4.169×10^{-5} (m^{-3})
0	1	1.6×10^{-2} (m^{-1})	5.12×10^{-5} (m^{-1})	4	0	6.975×10^{-3} (rad^{-4})	3.301×10^{-5} (rad^{-4})
2	0	-8.36×10^{-2} (rad^{-2})	-5.61×10^{-5}(rad^{-2})	3	1	-2.248×10^{-2} (m^{-1} rad^{-3})	-6.300×10^{-5} (m^{-1} rad^{-3})
1	1	-5.34×10^{-2} (m^{-1} rad^{-1})	4.15×10^{-5} (m^{-1} rad^{-1})	2	2	1.438×10^{-3} (m^{-2} rad^{-2})	6.290×10^{-5} (m^{-2} rad^{-2})
0	2	-6.56×10^{-3} (m^{-2})	4.81×10^{-5} (m^{-2})	1	3	5.909×10^{-3} (m^{-3} rad^{-1})	-2.915×10^{-5} (m^{-3} rad^{-1})
3	0	1.61×10^{-4} (rad^{-3})	-5.26×10^{-5} (rad^{-3})	0	4	3.473×10^{-4} (m^{-4})	7.007×10^{-6} (m^{-4})
2	1	5.09×10^{-2} (m^{-1} rad^{-2})	9.54×10^{-5} (m^{-1} rad^{-2})				

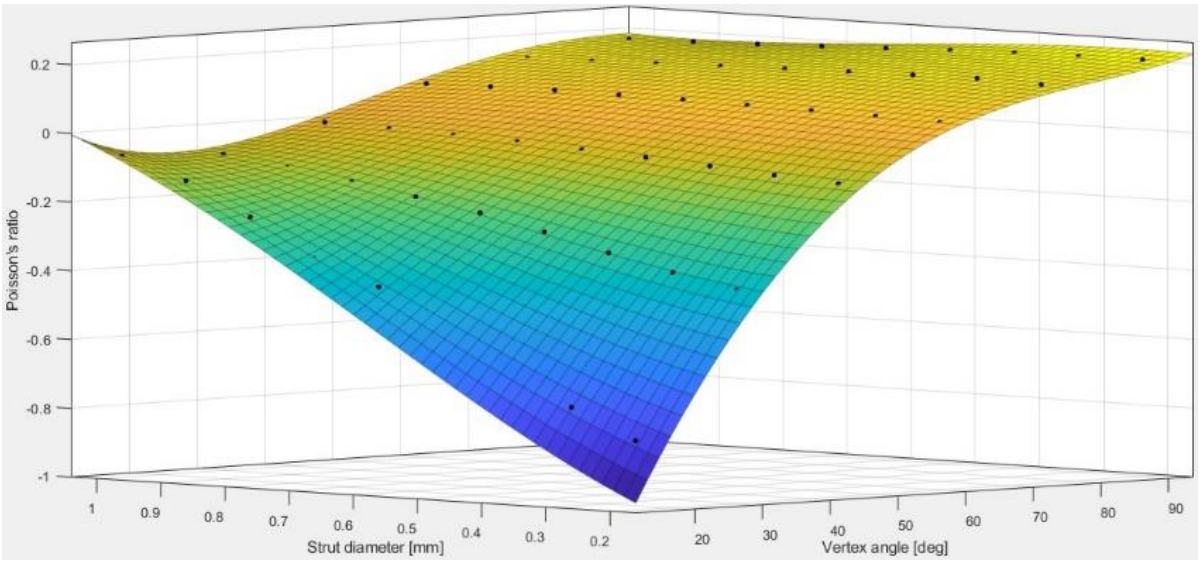

Figure 9. Plot of the fitted function for the Poisson's ratio of the structure against vertex angle and strut diameter.

Figure 9 clearly illustrates the effects of the two studied parameters on the Poisson's ratio of the structure. With the reduction in the strut diameter, the negative Poisson's ratio becomes greater. This was evident for the star-shaped lattice structures with vertex angles less than 60°. For structures with larger vertex angles, the effect was inconspicuous. This is an indication that the Poisson's ratio values became more sensitive to the change in strut dimeter for the lattice structures with relatively small vertex angles, which could

potentially be taken advantage of in engineering designs. Furthermore, as shown in Figure 10, the influence of the design parameters on the effective elastic modulus is obvious. It is clear that the effective modulus of the structure increases as the strut diameter increases and/or the vertex angle decreases. This demonstrates that it is possible to control the star-shaped lattice structure's stiffness through adjusting its design parameters.

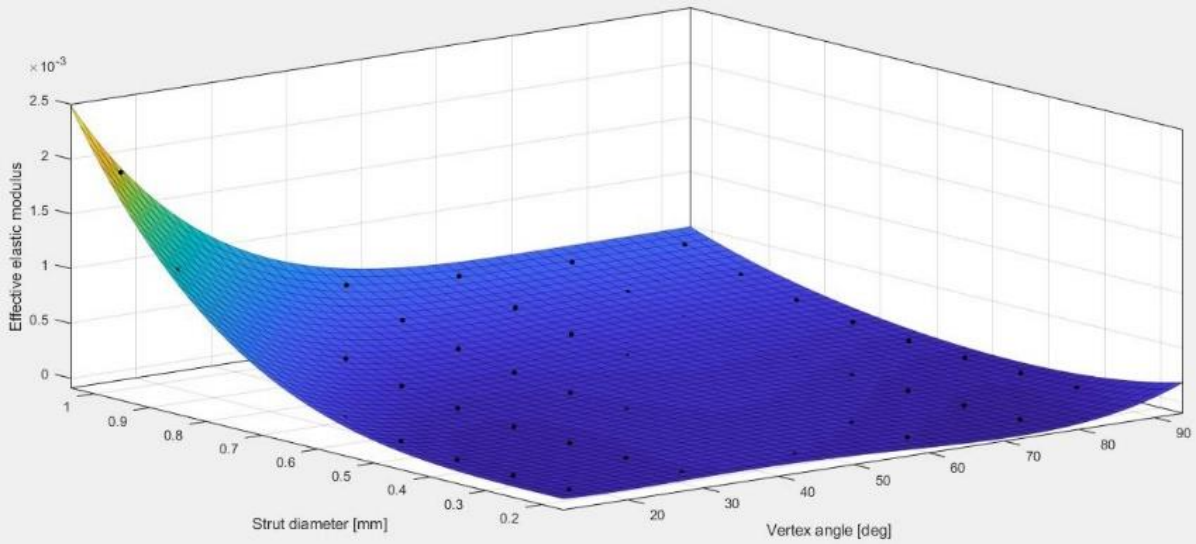

Figure 10. Plot of the fitted function for the effective elastic modulus of the structure against vertex angle and strut diameter.

3.2. Experimental

To validate the FEA results, three structures with different unit cell dimensions were evaluated after being additively built using the LPBF process. The vertex angles and strut dimeters of the structures were $\theta = 75°$ and D = 0.5 mm; $\theta = 50°$ and D = 0.5 mm; and $\theta = 40°$ and D = 0.5 mm. These parameters were specifically designed to produce star-shaped lattice structures with, correspondingly, positive, zero, and negative Poisson's ratios. Afterward, these star-shaped lattice structure designs were 3D-printed and compressed. An example of the star-shaped lattice structures made of Ti_6Al_4V that was produced for this investigation is shown in Figure 11a. In the initial experiments, the samples had already experienced some compressions with mild displacements delivered from different directions during the support removal process. However, when using star-shaped lattice structures with thinner interior supports, the supports were successfully snapped out of place without damaging or compressing the lattice structures (Figure 11b). The samples were then examined after excluding the impact of the supports.

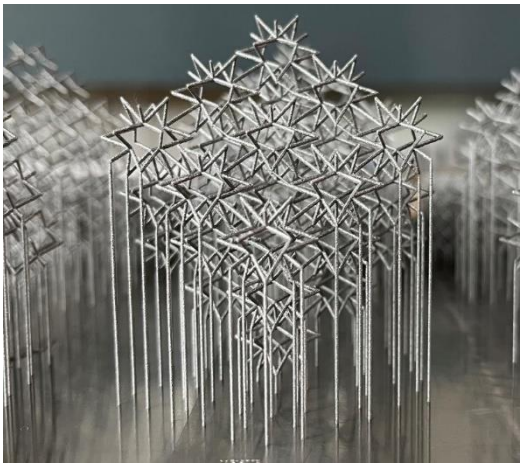

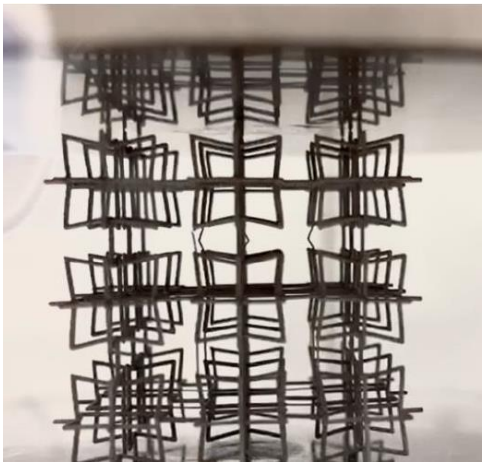

(**a**) (**b**)

Figure 11. (**a**) A sample of the Ti6Al4V LPBF-fabricated star-shaped lattice structures in this study. (**b**) Internal support failure observed during compression testing.

The compressive stress–strain diagrams for various star-shaped lattice configurations were created using the force and displacement data obtained from the compression experiments performed on three different star-shaped lattice structures with variable geometrical parameters, as shown in Figure 12. In order to enable a comparative evaluation of the mechanical properties of the star-shaped lattice structures, the FEA compression test results for the same three star-shaped lattice designs were also overlaid on the stress–strain diagrams in Figure 12. The purpose of this comparison was to validate the FEA results and confirm the precision of the designs produced using the FEA model. For lattices with a strut diameter of 0.5 mm and vertex angles of 50° and 75°, a strong agreement between the FEA and experimental data was observed. In contrast, the FEA predictions and the experimental results for the star-shaped lattice structure with a vertex angle of 40° and a strut diameter of 0.5 mm showed a deviation of about 10%. The close agreement between the experimental and simulation results indicates the accuracy of the model in estimating the properties of the star-shaped honeycomb structures investigated in this study.

The results of the current work could be a confirmation of earlier findings reported by Yang et al. [22], who studied the relationship between the geometrical design parameters and mechanical properties of 3D re-entrant-lattice auxetic structures. The cited authors reported that there were significant effects of the structural dimensions and the re-entrant angle on the Poisson's ratio and Young's modulus of the structure. In addition, it was suggested that when the number of unit cells is greater than or equal to three, the effect of size on the accuracy of the results can effectively be neglected, which was also confirmed in the current work. This is particularly useful for many practical design applications in which the number of unit cells is restricted due to overall component size.

Similar conclusions were also reported by Rad et al. [23] during their study of the factors controlling the mechanical properties of star-shaped lattice cellular structures. The authors indicated that varying the wall lengths, cell wall thickness, and angle of the structure's topology would provide the designer with more degrees of freedom with which to control the stiffness and Poisson's ratio of these cellular structures.

(a)

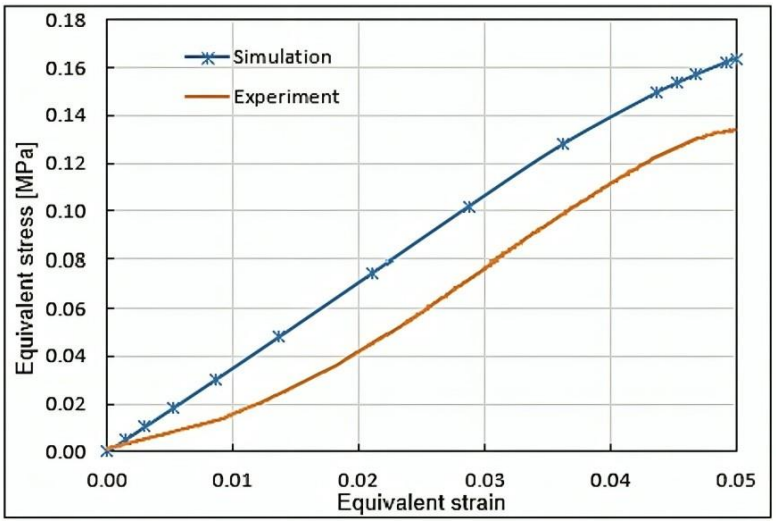

(b)

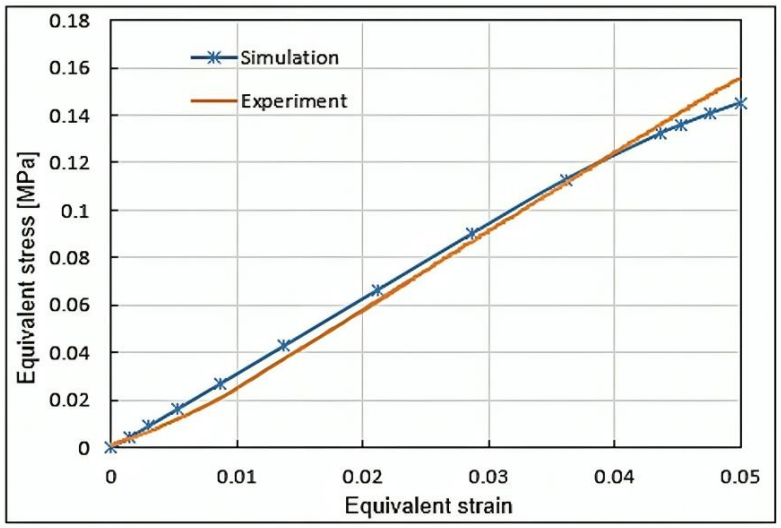

(c)

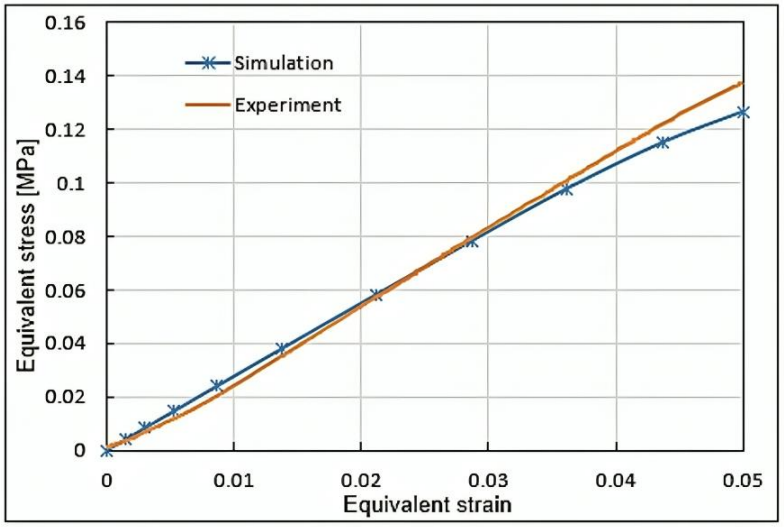

Figure 12. Comparison of the equivalent stress–strain curves from experiment and simulation of the star-shaped lattice structures with the following parameters: (**a**) θ = 40°, D = 0.5 mm; (**b**) θ = 50°, D = 0.5 mm; (**c**) θ = 75°, D = 0.5 mm.

3.3. Error Analysis

A comparison with experimental data was made to assess the accuracy of the FEA-predicted mechanical properties of the printed star-shaped lattice structures. The effective elastic modulus and Poisson's ratio experimental data for the three printed structures are summarised in Table 4. For each of the three designs, three structures were printed and subjected to a compression test. To assess the simulation error, the modelling results for the three lattice structures were also included and compared with the experimental findings. Among the three studied lattice structures, the effective elastic moduli (E/E^*) derived from the finite element analysis demonstrated an acceptable dependability, with a maximum error of 4.08%.

Regarding the Poisson's ratio (ν), star-shaped lattice structures with the indicated parameters ((θ = 75°, D = 0.5 mm), (θ = 50°, D = 0.5 mm), and (θ = 40°, D = 0.5 mm)) were shown to exhibit negative, zero, and positive Poisson's ratios, respectively. The simulation inaccuracy was, nonetheless, comparatively notable. There are several possible explanations for this divergence. Initially, there may have been a degree of error added since the use of the mechanical characteristics of the Ti_6Al_4V alloy in the simulation was based on literature research rather than experimental testing. Although data found in the literature is frequently trustworthy, differing production techniques and alloy compositions might result in differences in material quality. Additionally, the mechanical properties of the

star-shaped lattice structures may have been impacted by manufacturing flaws that are frequently encountered throughout the LPBF process. Furthermore, because of the geometric complexity of the star-shaped lattice structures, it was difficult to completely avoid shallow angles in certain struts even with careful rotation during the printing process. This could lead to imperfections in the printed structures that could result in weaker connections and reduced overall structural integrity, which could then lead to mechanical properties that are lower than expected.

The loading conditions during testing are another possible cause of the observed deviation. The force transmission along these contacting struts may not be completely vertical since there are only nine thin struts that make direct contact with the top or bottom surfaces of the testing equipment. As a result, during the compression test, there could have been some bending or misalignment. This implies that the star-shaped lattice structures might not have been compressed into an ideal upright position, which would lead to less accurate stress–strain correlations. Face plates on the top and bottom surfaces could be added as a potential solution to this issue. This would be especially useful for models with a higher number of unit cells. The stability of the structures under compressive stresses would be improved as a result.

Table 4. Errors of the simulation results compared to those from the experiment.

θ (°)	D (mm)	Properties	Experiment 1	Experiment 2	Experiment 3	Average	Simulation	Error (%)
40	0.5	ν	−0.114	−0.123	−0.133	−0.123	−0.108	12.20
40	0.5	E/E^* (×10^{-5})	2.955	3.112	3.008	3.038	3.116	2.57
50	0.5	ν	0	0.004	0.005	0.005	0.003	31.70
50	0.5	E/E^* (×10^{-5})	2.772	2.926	2.903	2.867	2.750	4.08
75	0.5	ν	0.143	0.114	0.138	0.132	0.161	21.97
75	0.5	E/E^* (×10^{-5})	2.447	2.431	2.552	2.477	2.380	3.92

3.4. Hybrid Unit Cells

The purpose of this study is to determine how the strut diameter and vertex angle affect the Poisson's ratio and effective elastic moduli of a star-shaped lattice structure. This suggests that each mechanical property has a single design solution that corresponds to particular values of the design parameters. This is a result of the fact that only two variables were examined. However, when taking into account other mechanical properties, a more thorough analysis with several variables would be needed. The star-shaped lattice structure configuration is an important factor to include. The star-shaped lattice structure, for instance, can be made up of several unit cell types. Every unit cell type has different design parameters that make distinct contributions to the structure's overall mechanical properties. Furthermore, changes in the number of struts or geometric arrangements can effectively broaden the range of the structure's mechanical characteristics.

Additive manufacturing can be used to tailor designs and modify unit cell arrangement, which can result in a variety of mechanical behaviours that affect stiffness, strength, and ductility. Therefore, it becomes essential to investigate the consequences of considering various lattice configurations, including variations in unit cell shape, arrangement, and size, in order to completely program, control, and optimise the mechanical performance of star-shaped lattice structures. For instance, merging two types of unit cells within a 3 × 3 × 3 (27 unit cells) structure can result in up to 14 distinct configurations while retaining isotropy (see Figure 13). As demonstrated, the following design configurations can be realised (as shown in Figure 13) if there are two distinct unit cell designs, A and B, which would be represented by the blue and white blocks, respectively, where there are 3 × 3 × 3 unit cells (27 units):

1. A unit cell of the A type in the centre of the cube (a structure consisting of 1 unit cell of type A and 26 unit cells of type B)—Figure 13a, Hybrid 1;

2. Unit cells of the A type at the centres of the faces (a structure consisting of 6 unit cells of the A type and 21 unit cells of the B type)—Figure 13b, Hybrid 2;
3. Unit cells of the A type at the centres of the faces and the cube (a structure consisting of 7 unit cells of the A type and 20 unit cells of the B type)—Figure 13b, Hybrid 3;
4. Unit cells of the A type at the vertices (a structure consisting of 8 unit cells of the A type and 19 unit cells of the B type)—Figure 13c, Hybrid 4;
5. Unit cells of the A type at the vertices and the centre of the cube (a structure consisting of 9 unit cells of the A type and 18 unit cells of the B type)—Figure 13c, Hybrid 5;
6. Unit cells of the A type in the middle of the edges (a structure consisting of 12 unit cells of the A type and 15 unit cells of the B type)—Figure 13d, Hybrid 6;
7. Unit cells of the A type in the middle of the edges and at the centre of the cube (a structure consisting of 13 unit cells of the A type and 14 unit cells of the B type)—Figure 13d, Hybrid 7.

It should be noted that if the white and blue blocks were swapped for the identical configurations shown above, there would be an additional seven possible combinations.

In order to demonstrate the possibility of customising the mechanical properties of a star-shaped lattice structure made up of two different unit cells, the fifth configuration was chosen from the available alternatives (see Figure 13c).

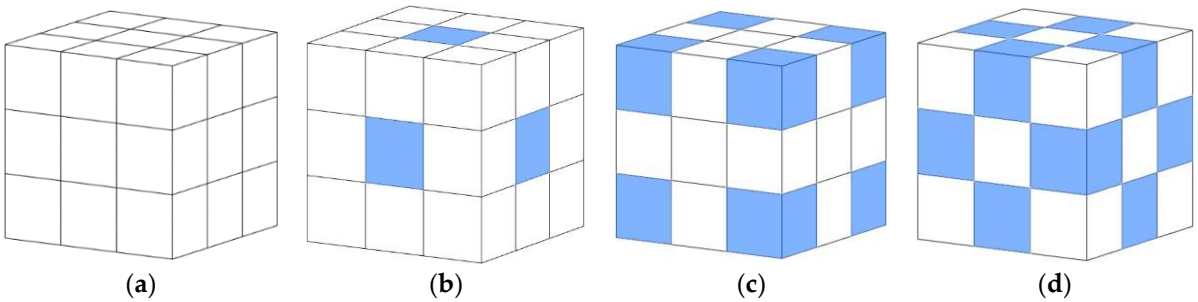

Figure 13. Possible arrangements of a 3 × 3 × 3 star-shaped lattice structure consisting of two different types of unit cells symbolized by the white and blue cubes. (**a**) Hybrid 1 (**b**) Hybrid 2,3 (**c**) Hybrid 5 (**d**) Hybrid 6,7.

The strut length of the two unit cells (the blue and white blocks in Figure 13c) was 0.5 mm, while the vertex angles was changed from 15 to 75°. The simulation results of the derived Poisson's ratio and effective elastic modulus versus the vertex angle of the blue block for a range of values of the vertex angle of the white block are shown in Figure 14a,b.

These findings suggest the possibility of tailoring the mechanical properties of star-shaped lattice structures by including unit cells of various sizes and configurations within the same structure. This would make it possible to construct star-shaped lattice structures with unique characteristics that are appropriate for use in a variety of industries, including the automotive, aerospace, defence, and medical sectors.

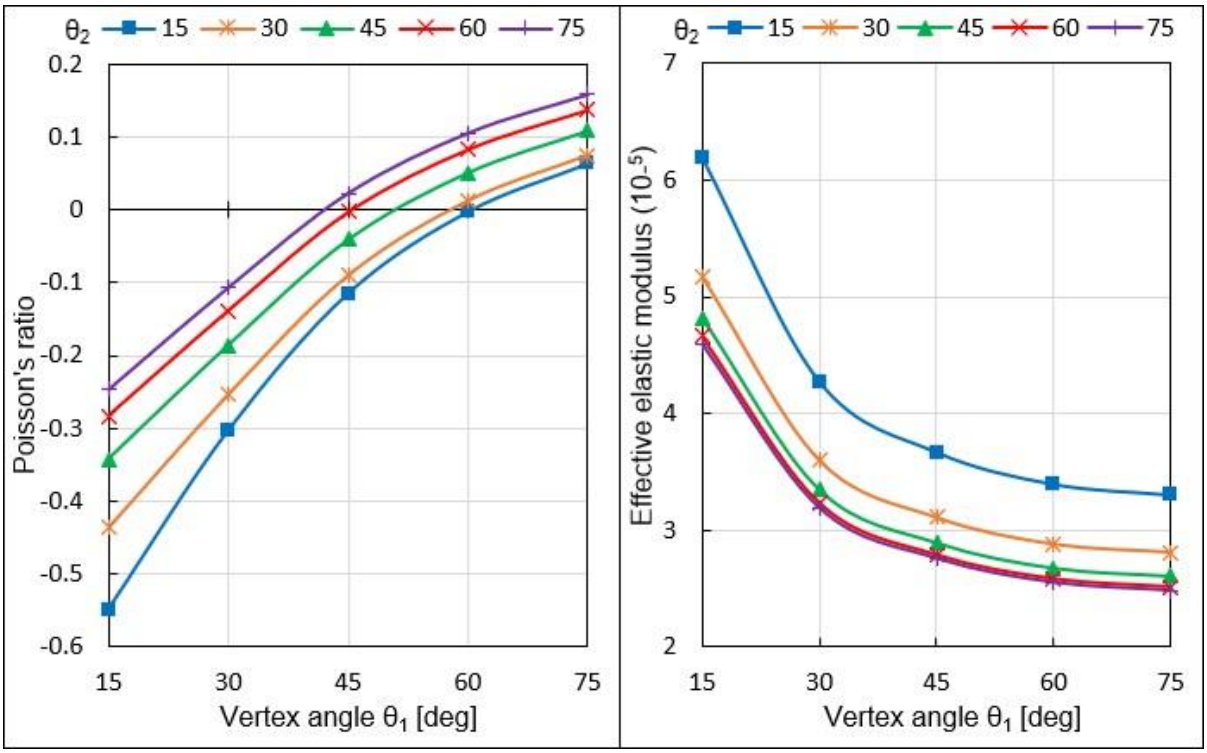

(**a**) (**b**)

Figure 14. (**a**) Poisson's ratio and (**b**) effective elastic modulus of the structures consisting of unit cells with a constant strut diameter of 0.5 mm but with two different angles.

4. Conclusions

This study investigated the development of a 3D star-shaped lattice structure fabricated from Ti6Al4V alloy and studied the impact of two key unit cell design parameters, namely, the vertex angle and strut diameter, on this structure's compressive properties, particularly its effective elastic modulus and Poisson's ratio. To clarify this relationship, experimental investigations and numerical simulations were conducted for a range of lattice structures designs. The star-shaped vertex angle was altered from 15 to 90 degrees, whereas the strut diameter was varied from 0.2 to 1 mm. This resulted in a wide variety of effective elastic moduli that ranged from 6×10^{-7} to 1.1×10^{-3}. Furthermore, variations in the unit cell dimensions resulted in fluctuations in the Poisson's ratio within the range of −0.8 to 0.2. Generally, the value of the vertex angle was shown to determine the Poisson's ratio's sign and behaviour (i.e., positive, zero, or negative). On the other hand, changing the strut diameter reduced this effect. The FEA results were validated against the additively manufactured titanium structures when subjected to compressive tests. Despite slight modelling errors in some cases, likely attributed to manufacturing defects and testing techniques, the FEA model demonstrated validity and therefore can be effectively applied to assess and predict the mechanical properties of star-shaped lattice structures. The FEA models also indicated that it was possible to provide better control and increased customization of the mechanical properties of the lattice structures by hybridizing them in a single structure. This could be achieved by combining two or more unit cells of different design parameters into a single design, allowing the structure to effectively meet specific requirements for various applications.

Author Contributions: Conceptualization, K.E.; Methodology, Y.W.; Validation, M.A.E.-S., K.E.; Formal analysis, H.H., J.D., M.A.E.-S. and N.A.A.; Resources, M.A.E.-S., N.A.A. and J.D.; Writing—original draft, Y.W., H.H. and M.A.E.-S.; Writing—review & editing, H.H., K.E., M.A.E.-S., J.D., M.A.E.-S., N.A.A.; Funding acquisition, J.D., M.A.E.-S., N.A.A. All authors have read and agreed to

the published version of the manuscript. All authors have read and agreed to the published version of the manuscript.

Funding: This work was supported and funded by the Deanship of Scientific Research at Imam Mohammad Ibn Saud Islamic University (IMSIU) (grant number IMSIU-RG23141).

Data Availability Statement:. The data presented in this study are available on request from the corresponding author.

Acknowledgments: The authors extend their appreciation to the Deanship of Scientific Research at Imam Mohammad Ibn Saud Islamic University (IMSIU) for funding and supporting this work through grant number IMSIU-RG23141.

Conflicts of Interest: The authors of this article declare that they have no conflicts of interest regarding the publication of this manuscript.

References

1. Lim, T.-C. *Mechanics of Metamaterials with Negative Parameters*; Springer Nature: Berlin/Heidelberg, Germany, 2020
2. Lakes, R.S. Negative-Poisson's-Ratio Materials: Auxetic Solids. *Annu. Rev. Mater. Res.* **2017**, *47*, 63–81.
3. Grima, J.N.; Evans, K.E. Auxetic behavior from rotating squares. *J. Mater. Sci. Lett.* **2000**, *19*, 1563–1565.
4. Karathanasopoulos; Rodopoulos, D.C. Enhanced Cellular Materials through Multiscale, Variable-Section Inner Designs: Mechanical Attributes and Neural Network Modeling. *Materials* **2022**, *15*, 3581. https://doi.org/10.3390/ma15103581.
5. Rafsanjani, A. and D. Pasini, Bistable auxetic mechanical metamaterials inspired by ancient geometric motifs. *Extrem. Mech. Lett.* **2016**, *9*, 291–296.
6. El-Sayed, M.A.; Essa, K.; Ghazy, M.; Hassanin, H. Design optimization of additively manufactured titanium lattice structures for biomedical implants. *Int. J. Adv. Manuf. Technol.* **2020**, *110*, 2257–2268.
7. Ghavidelnia; Bodaghi, M.; Hedayati, R. Idealized 3D Auxetic Mechanical Metamaterial: An Analytical, Numerical, and Experimental Study. *Materials* **2021**, *14*, 993. https://doi.org/10.3390/ma14040993.
8. Hassanin; Abena, A.; Elsayed, M.A.; Essa, K. 4D printing of NiTi auxetic structure with improved ballistic performance. *Micromachines* **2020**, *11*, 745.
9. Rogers, G.J.; Milthorpe, B.K.; Muratore, A.; Schindhelm, K. Measurement of the mechanical properties of the ovine anterior cruciate ligament bone-ligament-bone complex: A basis for prosthetic evaluation. *Biomaterials* **1990**, *11*, 89–96.
10. Shirzad; Zolfagharian, A.; Bodaghi, M.; Nam, S.Y. Auxetic metamaterials for bone-implanted medical devices: Recent advances and new perspectives. *Eur. J. Mech. A Solids* **2023**, *98*, 104905.
11. Kim; Son, K.H.; Lee, J.W. Auxetic Structures for Tissue Engineering Scaffolds and Biomedical Devices. *Materials* **2021**, *14*, 6821.
12. Abd-Elaziem, W.; Elkatatny, S.; Abd-Elaziem, A.-E.; Khedr, M.; El-baky, M.A.A.; Hassan, M.A.; Abu-Okail, M.; Mohammed, M.; Järvenpää, A.; Allam, T. On the current research progress of metallic materials fabricated by laser powder bed fusion process: A review. *J. Mater. Res. Technol.* **2022**, *20*, 681–707.
13. Khorasani; Gibson, I.; Ghasemi, A.H.; Hadavi, E.; Rolfe, B. Laser subtractive and laser powder bed fusion of metals: Review of process and production features. *Rapid Prototyp. J.* **2023**, *29*, 935–958.
14. *ASTM F2792-12a*; Standard Terminology for Additive Manufacturing Technologies. ASTM International, West Conshohocken, USA, 2014.
15. Essa; Sabouri, A.; Butt, H.; Basuny, F.H.; Ghazy, M.; El-Sayed, M.A. Laser additive manufacturing of 3D meshes for optical applications. *PLoS ONE* **2018**, *13*, e0192389.
16. Bittredge, O.H.H.; El-Sayed, M.A.; Eldessouky, H.M.; Alsaleh, N.A.; Alrasheedi, N.H.; Essa, K.; Ahmadein, M. Fabrication and Optimisation of Ti-6Al-4V Lattice-Structured Total Shoulder Implants Using Laser Additive Manufacturing. *Materials* **2022**, *15*, 3095.
17. Maconachie; Leary, M.; Lozanovski, B.; Zhang, X.; Qian, M.; Faruque, O.; Brandt, M. SLM lattice structures: Properties, performance, applications and challenges. *Mater. Des.* **2019**, *183*, 108137.
18. Zhang, X.Z.; Leary, M.; Tang, H.P.; Song, T.; Qian, M. Selective electron beam manufactured Ti-6Al-4V lattice structures for orthopedic implant applications: Current status and outstanding challenges. *Curr. Opin. Solid State Mater. Sci.* **2018**, *22*, 75–99.
19. Zadeh, N.; Dayyani, I.; Yasaee, M. Fish Cells, a new zero Poisson's ratio metamaterial—Part I: Design and experiment. *J. Intell. Mater. Syst. Struct.* **2020**, *31*, 1617–1637.
20. Gong; Ren, C.; Sun, J.; Zhang, P.; Du, L.; Xie, F. 3D Zero Poisson’s Ratio Honeycomb Structure for Morphing Wing Applications. *Biomimetics* **2022**, *7*, 198. https://doi.org/10.3390/biomimetics7040198.
21. Baertsch; Ameli, A.; Mayer, T. Finite-Element Modeling and Optimization of 3D-Printed Auxetic Reentrant Structures with Stiffness Gradient under Low-Velocity Impact. *J. Eng. Mech.* **2021**, *147*, 04021036.
22. Yang; Harrysson, O.; West, H.; Cormier, D. Mechanical properties of 3D re-entrant honeycomb auxetic structures realized via additive manufacturing. *Int. J. Solids Struct.* **2015**, *69*, 475–490.
23. Rad, S.; Ahmad, Z.; Alias, A. Computational approach in formulating mechanical characteristics of 3D star honeycomb auxetic structure. *Adv. Mater. Sci. Eng.* **2015**, *2015*, 650769.

24. Strek; Matuszewska, A.; Jopek, H. Finite Element Analysis of the Influence of the Covering Auxetic Layer of Plate on the Contact Pressure. *Phys. Status Solidi B* **2017**, *254*, 1700103.
25. Mrozek; Strek, T. Numerical Analysis of Dynamic Properties of an Auxetic Structure with Rotating Squares with Holes. *Materials* **2022**, *15*, 8712. https://doi.org/10.3390/ma15248712.
26. Bilski; Pigłowski, P.M.; Wojciechowski, K.W. Extreme Poisson's Ratios of Honeycomb, Re-Entrant, and Zig-Zag Crystals of Binary Hard Discs. *Symmetry* **2021**, *13*, 1127. https://doi.org/10.3390/sym13071127.
27. Bartolomeu; Gasik, M.; Silva, F.S.; Miranda, G. Mechanical Properties of Ti6Al4V Fabricated by Laser Powder Bed Fusion: A Review Focused on the Processing and Microstructural Parameters Influence on the Final Properties. *Metals* **2022**, *12*, 986. https://doi.org/10.3390/met12060986.
28. Cuadrado; Yánez, A.; Martel, O.; Deviaene, S.; Monopoli, D. Influence of load orientation and of types of loads on the mechanical properties of porous Ti_6Al_4V biomaterials. *Mater. Des.* **2017**, *135*, 309–318.
29. Lee, Y.T.; Peters, M.; Welsch, G. Elastic moduli and tensile and physical properties of heat-treated and quenched powder metallurgical Ti-6Al-4V alloy. *Metall. Trans. A* **1991**, *22*, 709–714.
30. Li, S.; Sitnikova, E., Eds. Chapter 1—Introduction—Background, Objectives and Basic Concepts. In *Representative Volume Elements and Unit Cells*; Woodhead Publishing: Sawston, UK, 2020; pp. 3–10.
31. *ASTM B822-15*; Standard test method for particle size distribution of metal powders and related compounds by light scattering. ASTM International, West Conshohocken, USA, 2015.
32. Farashi; Vafaee, F. Effect of printing parameters on the tensile strength of FDM 3D samples: A meta-analysis focusing on layer thickness and sample orientation. *Prog. Addit. Manuf.* **2022**, *7*, 565–582.